Interaction of the 20 kDa and 63 kDa Fragments of Anthrax Protective Antigen: Kinetics and Thermodynamics †

ARTICLE *in* BIOCHEMISTRY · FEBRUARY 2005

Impact Factor: 3.02 · DOI: 10.1021/bi047791s · Source: PubMed

4 AUTHORS:

Kenneth A Christensen
Brigham Young University - Provo Main Cam…
40 PUBLICATIONS **1,650** CITATIONS

SEE PROFILE

Bryan A Krantz
University of Maryland, Baltimore
46 PUBLICATIONS **2,587** CITATIONS

SEE PROFILE

Roman A Melnyk
SickKids
35 PUBLICATIONS **1,170** CITATIONS

SEE PROFILE

Robert John Collier
Harvard Medical School
269 PUBLICATIONS **17,069** CITATIONS

SEE PROFILE

Interaction of the 20 kDa and 63 kDa Fragments of Anthrax Protective Antigen: Kinetics and Thermodynamics†

Kenneth A. Christensen,‡ Bryan A. Krantz,‡ Roman A. Melnyk, and R. John Collier*

Department of Microbiology and Molecular Genetics, Harvard Medical School, 200 Longwood Avenue, Boston, Massachusetts 02115

Received October 15, 2004

ABSTRACT: The action of anthrax toxin begins when the protective antigen (PA_{83}, 83 kDa) moiety binds to a mammalian cell-surface receptor and is cleaved by a furin-family protease into two fragments: PA_{20} (20 kDa) and PA_{63} (63 kDa). After PA_{20} dissociates, receptor-bound PA_{63} spontaneously oligomerizes to form a heptameric species, which is able to bind the two enzymatic components of the toxin and transport them to the cytosol. Treatment of PA_{83} with trypsin yielded PA_{63} and a form of PA_{20} lacking unstructured regions at the N- and C-termini. We labeled these fragments with dyes capable of fluorescence resonance energy transfer to quantify their association in solution. We kinetically determined that the equilibrium dissociation constant is 190 nM with a dissociation rate constant, k_{off}, of 3.3×10^{-2} s^{-1} ($t_{1/2}$ of 21 s). A two-step association process was observed using stopped-flow: a fast bimolecular step ($k_{on} = 1.4 \times 10^5$ M^{-1} s^{-1}) was followed by a slower unimolecular step ($k = 3.5 \times 10^{-3}$ s^{-1}) with an equilibrium isomerization constant, K_{iso}, of 2.1. The two-step mechanism most consistent with the data is one in which the dissociation of the PA_{20}·PA_{63} complex is followed by an isomerization in the PA_{63} moiety. Our results indicate that, following the cleavage of PA on the cell surface, PA_{20} is largely dissociated within a minute. A slow isomerization step in PA_{63} may then potentiate it for oligomerization and subsequent steps in toxin action.

Anthrax toxin, a major virulence factor of *Bacillus anthracis*, consists of three nontoxic proteins that interact on the surface of mammalian cells to form toxic noncovalent complexes (*1*, *2*). The three proteins are as follows: edema factor (EF), a Ca^{2+}- and calmodulin-dependent adenylate cyclase; lethal factor (LF), a Zn^{2+}−metalloprotease; and protective antigen (PA_{83}, 83 kDa), a protein that binds EF, LF, or both and delivers them to the cytosol of mammalian cells. Once within the cytosol, EF and LF contact their substrates and catalyze reactions that result in toxicity (*3*−*5*).

Anthrax toxin assembly and action begin when PA_{83} binds to either of two known cell surface receptor proteins: anthrax toxin receptor/tumor endothelial marker-8 (ATR/TEM8) or capillary morphogenesis protein 2 (CMG2) (*6*, *7*). A cellular protease of the furin family then cleaves PA_{83} into 2 fragments: PA_{20} (20 kDa), corresponding to the N-terminus, and PA_{63} (63 kDa), corresponding to the C-terminus (*8*). PA_{20} dissociates into the medium and plays no further known role in toxin action. This eliminates a steric barrier to self-association, allowing PA_{63} to oligomerize and form a heptameric ring-shaped structure called prepore (*9*). PA_{63} heptamer binds up to three molecules of LF or EF competitively and with nanomolar affinity (*10*, *11*). The resulting complexes are localized to detergent-resistant lipid microdomains, where they undergo receptor-mediated endocytosis (*12*). Acidification of the toxin-containing compartment then causes a structural rearrangement of the prepore that enables it to insert into the membrane and form a pore (*13*, *14*). Pore formation is linked to translocation of the bound enzymatic cargo (LF or EF) to the cytosol, but the mechanism of translocation remains poorly understood. LF has been shown to cleave members of the mitogen-activated protein kinase kinase family (*4*, *5*), leading, by a still poorly defined sequence of events, to host death. Elevation of cAMP concentration by EF may protect the bacteria from degradation by macrophages (*15*).

From this qualitative picture of anthrax toxin action, efforts are currently underway to characterize the kinetics and thermodynamics of interactions between toxin components. Here, we present studies of the noncovalent interaction between PA_{20} and PA_{63}, which occurs via the large hydrophobic interface observed in the crystallographic structure of PA_{83} (*9*). Our measurements in solution using fluorescence resonance energy transfer (FRET) suggest a mechanism for the dissociation of PA_{20} from PA_{63}, enabling better understanding of this early step in toxin assembly.

†This work was supported by NIH grant (R37-AI022021). R.J.C. holds equity in PharmAthene, Inc.

* To whom correspondence should be addressed. E-mail: jcollier@hms.harvard.edu. Telephone: (617) 432-1930. Fax: (617) 432-0115.)

‡ Co-first authors.

[1] *Abbreviations.* PA, Protective Antigen; PA_{83}, 83 kDa full length PA.; PA_{20}, 20 kDa fragment of PA.; PA_{63}, 63 kDa fragment of PA.; PA_{63}*, PA_{63} isomer unable to bind PA_{20}; FRET, fluorescence resonance energy transfer; EF, edema factor; LF, lethal factor; LF_N, N-terminal domain of LF.; nPA_{83}, nicked PA_{83}; nPA_{83} E465C*488, nPA_{83} where C465 in the PA_{63} moiety is labeled with a donor fluorophore (Alexa fluor 488); nPA_{83} Q140C*594, nPA_{83} where C140 in the PA_{20} moiety is labeled with an acceptor fluorophore (Alexa fluor 594); k_{off}, off-rate constant; k_{on}, on-rate constant; K_d, equilibrium dissociation constant; K_{iso}, equilibrium isomerization constant; Ex., excitation; Em., emission.

10.1021/bi047791s CCC: $30.25
Published on Web 12/30/2004

MATERIALS AND METHODS

Protein Expression and Purification. PA_{83} (wild type, T126C, Q140C, E465C, and K563C) and LF_N (residues 1 to 263 of LF) were produced recombinantly in *E. coli* BL-21 DE3 star using pET22b (for PA) and pET15b (for LF_N). Cultures were grown in a 5 L fermenter at 37 °C using ECPM1 growth media (*16*) supplemented with carbenicillin (50 mg/L) until reaching an OD_{600} of 3−10. After induction by IPTG (0.8−1 mM) for 3−4 h at 27−30 °C for PA_{83} and 37 °C for LF_N, cells grew to a final OD_{600} of 6−20. PA_{83} periplasmic lysates were generated as previously described (*17*). Periplasmic lysate was buffered with 20 mM Tris-Cl and supplemented with 2 mM dithiothreitol to protect free Cys sites. The PA_{83} periplasmic lysate was purified by Q Sepharose anion-exchange chromatography (Amersham) eluted by a 0 → 250 mM NaCl gradient, using buffers A (20 mM Tris−Cl, 1 mM $CaCl_2$, pH 8.5) and B (A + 1 M NaCl). For LF_N, cell pellets lysed by French press and sonication were purified as previously described using His-6 Ni^{2+}-affinity chromatography (*18*). Pure fractions (by SDS−PAGE) were concentrated to 30 g/L and stored at −80 °C. Protein concentrations were determined by absorbance (ϵ_{280} of 75670 and 18040 M^{-1} cm^{-1} for PA_{83} and LF_N, respectively.)

Preparation of nPA_{83} and Purification of PA_{20}. Nicked PA_{83} (nPA_{83}) was prepared with either TPCK-treated trypsin (Sigma) or furin (New England Biolabs). Trypsinization was carried out by incubating PA_{83} (1−2 mg/mL) in buffer C (15/85% mixture of buffers A and B) for 30 min at room temperature at a 1:1000 w/w ratio trypsin:PA, yielding > 90% nicking efficiency. Soybean trypsin-chymotrypsin inhibitor (Sigma) was added in a 10-fold w/w excess of trypsin to prevent further proteolysis. Furin proteolysis required incubating PA_{83} (1 mg/mL) in buffer C with 10 units of furin per mg of PA overnight at room temperature, yielding >90% nicking efficiency. PA_{20} was purified from the proteolysis reaction and PA_{63} by Q Sepharose (0 → 500 mM NaCl gradient, using buffers A and B). Fractions were pooled based on SDS−PAGE and further purified to >95% using Superdex 75 or Sephacryl 100 size exclusion chromatography in Buffer *C*. Protein concentrations were determined by absorbance (ϵ_{280} = 26030 $M^{-1}cm^{-1}$).

Fluorescent Labeling of PA. Proteins with single Cys mutations were labeled with Alexa fluor 488 C_5 maleimide or Alexa fluor 594 C_5 maleimide (Molecular Probes) using the manufacturer's procedures. Protein solutions were exchanged back into buffer C by gel filtration. Conjugates' dye:protein ratios were 0.9−1.2, and they were stored at −80 °C.

Off-Rate Measurements. Fluorescently labeled solutions, nPA_{83} E465C labeled with Alexa fluor 488 (nPA_{83} E465C*488) and nPA_{83} Q140C labeled with Alexa fluor 594 (nPA_{83} Q140C*594), were mixed at a 1:1 ratio in buffer C to a final nPA_{83} concentration of 12 μM. Solutions were incubated for 30 min at room temperature, allowing formation of nPA_{83} complexes wherein fluorescent labels were present in both the 20 kDa and 63 kDa moieties by random exchange. Upon reaching equilibrium, ∼25% of the nPA_{83} becomes doubly labeled with donor and acceptor fluorophores. Purified unlabeled PA_{20} was added in 10-fold excess to the doubly labeled 100 nM nPA_{83} complexes. Dissociation was reported by the reduction in FRET (em. ratio 615 to 520 ± 16 nm, ex. 488 nm Ar^+ laser line) using an ISS K2 spectrofluorimeter. Data were fit using single exponentials, $A(t) = A_o \exp(-kt) + c$, to recover the observed off-rate constant, k. Off-rates were also measured by rapid dilution of 12 μM double-labeled nPA_{83} to 1−100 nM while measuring reductions in FRET. All measurements were done at 20 °C.

On-Rate Measurements. Solutions of 10 nM nPA_{83} E465C*488 were incubated in buffer C for at least 15 min at 20 °C with stirring. At t_0, purified PA_{20} Q140C*594 was added to 100 nM or 1 μM to maintain pseudo-first-order conditions. In slow manual mixing experiments, increases in FRET (em. ratio 615 to 520 ± 16 nm, ex. 488 nm Ar^+ laser line) were recorded using the ISS spectrofluorimeter. For faster rate determinations, a Biologic SFM-400 stopped-flow was used as previously described (*19*). Association kinetics experiments were reported by FRET (em. ratio 520 ± 10 nm band-pass filter to >570 nm long-pass filter, Omega Optical; ex. 488 nm Ar^+ laser line). Protein solutions were diluted into Buffer *C* and temperature was maintained by a circulating water bath at 20 °C. Syringe 1 contained buffer alone. Syringes 2 and 3 contained 2 and 0.4 μM stock solutions of PA_{20} Q140C*546, respectively. Syringe 4 contained a 20 nM stock solution of nPA_{83} E465C*488. A constant volume (150 μL) of syringe 4 was delivered in each experiment, where the balance of the total shot volume, 300 μL, was delivered by the other syringe to vary the concentration of PA_{20}. Flow rates were 7−15 mL s^{-1}; the dead volume is 15 μL; and the dead time is 1−2 ms. Transients were fitted double-exponential decays, $A(t) = \Sigma A_{o,i} \exp(-k_i t) + c$, to recover association rate constants, k, and amplitudes, A_o.

Equilibrium K_d Determination. The affinity of the PA_{20}·PA_{63} interaction was measured by serial dilution of equimolar nPA83 E465C*488 and nPA83 Q140C*594 at 20 °C. Under these conditions, ∼25% of the nPA_{83} (PA_{20}·PA_{63} complex) is double-labeled. The observable FRET signal, θ, (em. ratio 615 to 520 ± 16 nm, ex. 488 nm Ar^+ laser line) was measured as the concentration varied from 1 μM to 1 nM using the ISS fluorimeter. Excitation intensity was controlled by the addition of neutral density filters to avoid photon counting pulse pile-up, and corrections for inner-filter effect were applied (*20*). θ_{max}, the signal of fully bound PA_{63}, was estimated by extrapolating amplitudes to t_0 from binding dissociation experiments. A single-site binding model, in which the binding partner, PA_{63}, isomerizes with a form unable to bind PA_{20}, called PA_{63}*, by the equilibrium rate constant, $K_{iso} = [PA_{63}^*]/[PA_{63}]$, is described by

$$\theta = \frac{\theta_{max}[PA_{20}]_{free}}{K_d(1 + K_{iso}) + [PA_{20}]_{free}} \quad (1)$$

Since free PA_{20} concentrations are related to total concentrations by $[PA_{20}]_{free} = [PA_{20}]_{total} \times (\theta_{max} - \theta)/\theta_{max}$ (when the unbound signal is set as zero), then the serial dilution data is able to be fit by

$$\theta = \theta_{max} + \frac{\theta_{max}K_d(1 + K_{iso})}{2[PA_{20}]_{total}}\left(1 - \sqrt{1 + \frac{4[PA_{20}]_{total}}{K_d(1 + K_{iso})}}\right) \quad (2)$$

The equilibrium dissociation data were fitted using the

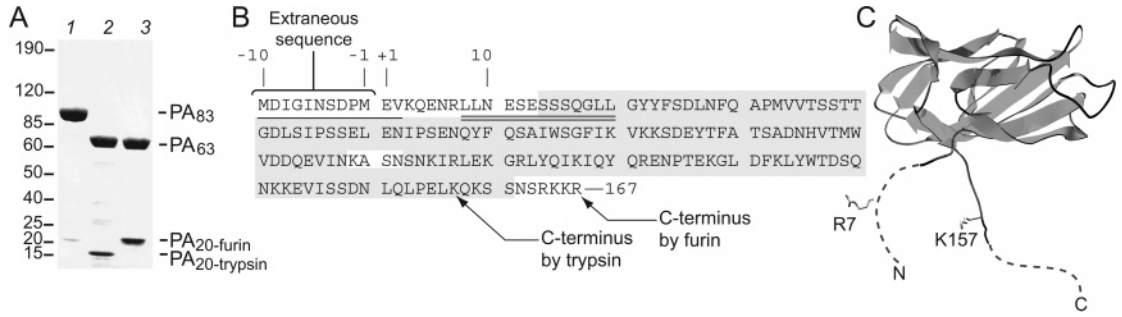

FIGURE 1: PA_{20} produced by trypsin and furin cleavage. (A) SDS−PAGE of nPA_{83} prepared with furin and trypsin with MW markers indicated in kDa at left: PA_{83} untreated (lane 1); PA_{83} treated with trypsin (lane 2) or furin (lane 3). (B) Amino acid sequence of PA_{20}, wherein the identified peptides by N-terminal Edman degredation for furin (*single underlined*) and trypsin (*double underlined*) cleavage are indicated. Extraneous N-terminal sequence is legacy of the expression clone used to produce PA_{83}. The indicated C-termini are deduced from mass spectrometry (Table 1). Residues shaded in gray are those that are ordered and present in the crystal structure of PA_{83}. (C) Ribbon diagram of the PA_{20} portion of the PA_{83} crystal structure (*9*). The N- and C-termini, which are disordered in the structure, are shown as dotted lines. R7 and K157 are highlighted as the N- and C-terminial trypsin cleavage sites in PA_{20}. Notice that PA_{20} prepared by furin cleavage only differs from that prepared by trypsinization in the highly disordered N-terminus and the C-terminal linker formerly connecting PA_{20} to PA_{63}.

Table 1: Mass Spectrometry and N-Terminal Sequencing of PA Nicked by Furin and Trypsin

protein	protease	expected[a] MW (Da)	measured[b] MW (Da)	N-···C-terminal residues of protein[c]
PA_{20}	trypsin[d]	17160	17145	L_8···K_{157}
PA_{20}	furin	20319	20013	M_{-10}···R_{167}[e]
PA_{63}	trypsin[d]	63448	63356	S_{168}···G_{735}

[a] Based on N-terminal sequencing by Edman degradation (Figure 1B) and the likely cleavage recognition site for the proteases. [b] Major peaks from MALDI mass-spectrometry are given. [c] See also Figure 1B. [d] TPCK-treated. [e] M_{-10} designates the inclusion of 10 extraneous residues on the N-terminus of furin cleaved PA_{20}.

kinetically determined parameters, K_{iso} and K_d, as fixed parameters to demonstrate consistency between the kinetic and equilibrium data.

Temperature Dependence of PA_{20} Dissociation. Dissociation rates, k_{off}, monitored by FRET were measured as a function of temperature, T, at 10, 20, 28, and 37 °C. k_{off} values were then fitted in an Eyring plot by

$$k_{off} = (k_B/h)\exp(\Delta^{\ddagger}S/R - \Delta^{\ddagger}H/RT), \qquad (3)$$

where R, k_B, and h are the gas, Boltzman, and Plank constants, respectively. $\Delta^{\ddagger}H$ and $\Delta^{\ddagger}S$ are the enthalpy and entropy of activation, respectively. $\Delta^{\ddagger}G$ was calculated by $\Delta^{\ddagger}G = \Delta^{\ddagger}H - T\Delta^{\ddagger}S$.

RESULTS

Preparation of PA_{20} by Proteolysis. We prepared PA_{20} from PA_{83} using two different proteases, trypsin and furin, and compared the products. Whereas the PA_{63} fragments from the different digestions were identical as judged by SDS−PAGE and mass spectrometry, the PA_{20} fragment from trypsin digestion was ~3 kDa smaller than that from furin digestion (Figure 1A; Table 1). Edman degradation showed that the tryptic fragment's N-terminus was truncated by 17 residues (Figure 1B), and mass spectrometry revealed that it also lacked 10 residues at the C-terminus (Table 1). Of the 17 residues missing from the N-terminus, the 10 most N-terminal are extraneous (not part of wild-type PA_{83}) and introduced by the cloning process. The next seven residues are part of the wild-type PA_{83} sequence but are not ordered

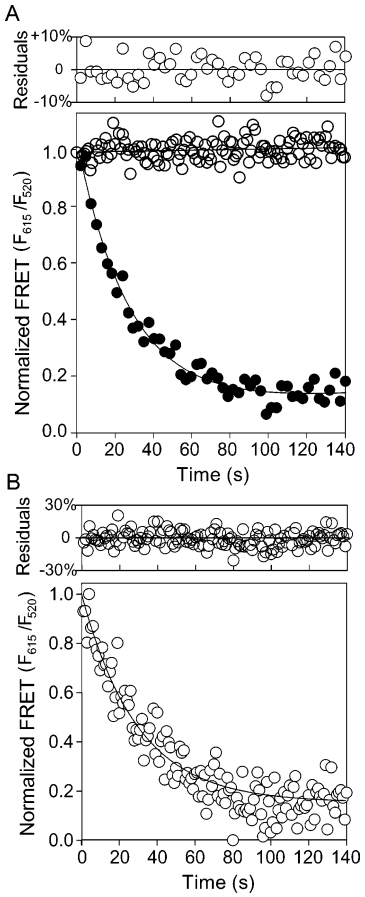

FIGURE 2: PA_{20} off-rate determination. Representative dissociation kinetics of PA_{20} from PA_{63}. (A) Trypsin nicked, doubly labeled nPA_{83} complex (E465C*488, Q140C*594) at 100 nM was competed with 1 μM unlabeled PA_{20} (solid circles) and without unlabeled PA_{20} (open circles, as a control), using FRET to report dissociation. (B) Furin nicked, doubly labeled nPA_{83} complex rapidly diluted from 12 to 1 μM. Curves, fitted to a single exponential, are the average of three experiments.

in the crystallographic structure of PA_{83} (Figure 1C). The 10 residues missing from the C-terminus are in the linker region between the PA_{20} and PA_{63} moieties and are also expected to be disordered in solution (Figure 1B,C). We showed (Figure 2) that the dissociation rates of the trypsin- and furin-derived forms of nPA_{83} are identical and used the

Table 2: PA_{20}·PA_{63} Complex Dissociation Rates at 20 °C

$[nPA_{83}]^a$ (nM)	$[PA_{20}]^b$ (μM)	$k_{off} \times 10^{-2}$ (s^{-1})
100	0.1	3.0 ± 0.2
100	1	3.3 ± 0.3
100	10	3.6 ± 0.1
10	0	3.1 ± 0.2
1	0	2.6 ± 0.3

[a] Double-labeled FRET complex. [b] Unlabeled competitor.

trypsin-derived fragment for most of the measurements reported.

Labeling nPA_{83} with Two Dyes Capable of FRET. To estimate the equilibrium and kinetic dissociation constants, doubly labeled nPA_{83} FRET complex was prepared. PA_{83}-E465C was labeled with Alexa fluor 488 (donor), and PA_{83}-Q140C with Alexa fluor 594 (acceptor). Equal parts of labeled PA_{83} proteins (PA_{83} Q140C*594 and PA_{83} E465C*488) were nicked with either trypsin or furin, mixed, and incubated to allow the PA_{20} moieties to exchange. Thus ~25% of the population of nPA_{83} molecules contained one of each label. Residues 140 and 465 are in PA_{20} and PA_{63}, respectively. Therefore, the complex exhibited FRET, because the dye pair is separated by ~40 Å and well within the 55 Å Förster distance expected for the dye pair.

Dissociation Kinetics of the PA_{20} Fragment. To measure the dissociation rate constant (k_{off}) for the labeled PA_{20}·PA_{63} complex prepared by trypsinization, we added a 10- to 100-fold molar excess of unlabeled wild-type PA_{20} to an equilibrated equimolar mixture of nPA_{83} E465C*488 and nPA_{83} Q140C*594, monitoring the FRET ratio as a function of time (Figure 2A). A consistent k_{off} of $3.3 \pm 0.3 \times 10^{-2}$ s^{-1} ($t_{1/2} = 21 \pm 2$ s) was observed at all concentrations of unlabeled PA_{20} tested. No change in FRET efficiency was seen in the absence of added competitor, PA_{20} (Figure 2A). A similar dissociation rate ($t_{1/2}$ of 24 ± 2 s; data not shown) was observed in the absence of unlabeled PA_{20} when the equilibrium is shifted toward dissociation by rapidly diluting the nPA_{83} FRET complex from 12 μM to 1−100 nM. As expected for a unimolecular dissociation process, no concentration dependence was observed (Table 2; Figure 3D). Finally, as a control for potential differences between the trypsin-treated PA_{83} and the physiologically relevant furin-treated PA_{83}, we measured the k_{off} of furin-treated doubly labeled nPA_{83} by rapid dilution from 12 μM to 1−100 nM (Figure 2B). The k_{off} value for the furin-treated PA_{83} was $3.4 \pm 0.4 \times 10^{-2}$ s^{-1}, demonstrating no difference in dissociation kinetics (Figure 2B).

Binding Association Kinetics of PA_{20} and PA_{63}. To measure the association rate constant (k_{on}), a solution of nPA_{83} E465C*488 (labeled only on the PA_{63} fragment) was diluted to 10 nM, a concentration at which the complex was largely dissociated. Labeled PA_{20} was then added to give a final total concentration of PA_{20} of 20 nM to 1 μM, and the increase in the ratio of emission of donor and acceptor fluorophores was monitored with time. The association rates observed at low PA_{20} concentrations (≤100 nM) could be fit to a single-exponential, as expected for a single-step mechanism (Figure 3A). However, a double-exponential decay function was required to fit the data at higher PA_{20} concentrations (Figure 3B), indicating two kinetic steps. No change in fluorescence was seen if PA_{83} had not been proteolytically activated (Figure 3B), ruling out nonspecific interactions and mixing artifacts.

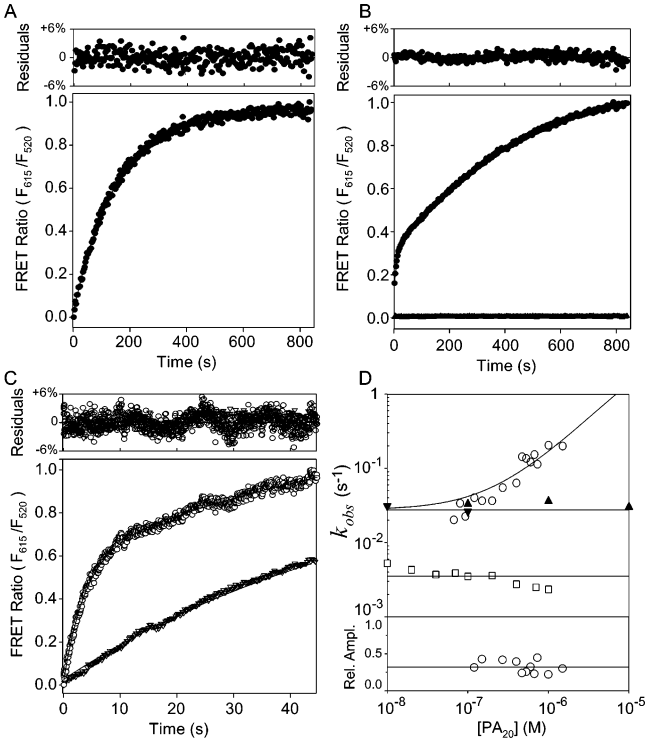

FIGURE 3: PA_{20} on-rate determination. Representative association kinetics of PA_{20}, where uncomplexed nPA_{83} E465C*488 (10 nM) is bound by (A) 100 nM and (B) 1 μM PA_{20} Q140C*594. In panels A and B, the data are the average of three experiments. Residuals are plotted above the fitted data. The lower (flat) trace represents a control with PA_{83} that had not been proteolytically activated. (C) Representative stopped-flow kinetic traces for the determination of the fast PA_{20} association rate. nPA_{83} E465C*488 (10 nM) is bound by PA_{20} Q140C*594 at either 80 nM (bottom trace) or 1 μM (upper trace). Each kinetic transient is the average of four shots. (D) Stopped-flow fast association rate constants (upper panel) of PA_{20} (open circles) and measured off-rates from competition experiments (triangles) and dilution (upside down triangles). A plot of the concentration dependence of the slow association step is also shown, as determined in manual mixing experiments (squares). At bottom is shown a concentration dependence of the fast amplitude relative to the total amplitude, $A_{fast}/(A_{fast} + A_{slow})$, where the average value is 32 ± 8%.

Stopped-flow measurements were used to obtain accurate values of the fast association rates at high PA_{20} concentrations. Because these measurements were performed at concentrations near the estimated K_d for the PA_{20}·PA_{63} complex, the observed association rate (k_{obs}) is given by

$$k_{obs} = [PA_{20}]k_{on} + k_{off} \quad (4)$$

In the limit of low PA_{20} concentrations, the observed rate of association approached the off-rate. We, therefore, fit the fast association rate data from the stopped flow measurements to eq 4 (Figure 3D). The fast k_{on} calculated from this approach was $1.4 \pm 0.1 \times 10^5$ $M^{-1}s^{-1}$; k_{off} was $2.8 \pm 0.6 \times 10^{-2}$ s^{-1} and in agreement with the previously determined value of $3.3 \pm 0.3 \times 10^{-2}$ s^{-1}. From these kinetic values, we calculated the equilibrium K_d of the PA_{20}·PA_{63} interaction ($K_d = k_{off}/k_{on}$) to be 190 ± 50 nM.

While the fast association rate changed significantly as a function of PA_{20} concentration, the slow association rate ($3.5 \pm 0.3 \times 10^{-3}$ s^{-1}) was independent of concentration (Figure

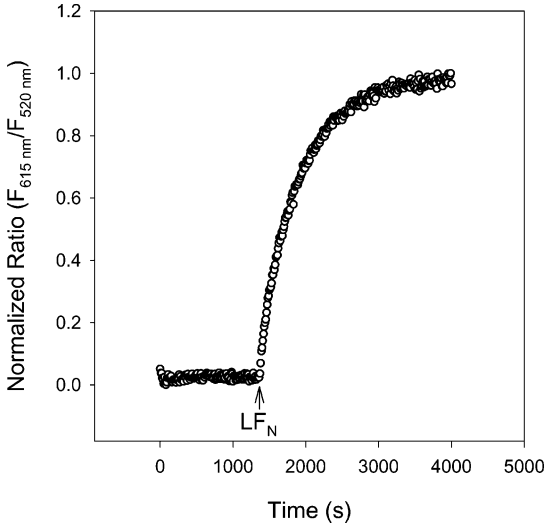

FIGURE 4: PA_{63} oligomerization. nPA_{83} K563C*488 and nPA_{83} K563C*594 were mixed (10 nM each), and the fluorescence emission ratio was monitored. At $t = 20$ min, 100 nM LF_N was added, prompting PA_{63} oligomerization, which is indicated by the increase in FRET.

3D). The existence of two separate kinetic steps is masked at the lowest PA_{20} concentrations, where concentration-dependent association of PA_{20} and PA_{63} is slow and similar to the rate-determining second step. At higher PA_{20} concentrations, where an association step is faster, the initial fast association step is more clearly separated from the slower step.

We also measured the amplitudes of the fast and slow kinetic phases, A_{fast} and A_{slow}, respectively. We found no concentration dependence on the relative amplitudes of these two distinct phases over the measured concentration range (Figure 3D). The fast phase was on average 32 ± 8% of the total amplitude. Assuming the slower phase appeared due to an isomerization step, we calculated the equilibrium constant, K_{iso}, as 2.1 ± 0.8 by $K_{iso} = A_{slow}/A_{fast}$.

To control for possible perturbations due to the presence of the fluorescent labels, we measured dissociation and association rates for the nPA_{83} complex at probe locations significantly removed from the PA_{20}·PA_{63} binding interface. The PA_{63} fragment was labeled at the K563C site with Alexa fluor 594, and the PA_{20} fragment was labeled at the T126C site with Alexa fluor 488. Measured dissociation and association kinetics were statistically indistinguishable from the previously measured rates (data not shown).

Oligomerization of PA_{63}. Since it is known that PA_{63} can spontaneously oligomerize following dissociation of PA_{20}, we conducted experiments to determine whether an oligomerization side reaction occurs under our experimental conditions, as this could impact the observed kinetics. Here, labeled and nicked Cys mutants nPA_{83} K563C*488 and nPA_{83} K563C*594 (labeled in the PA_{63} moiety) were used as FRET probes for oligomerization. Equimolar amounts of labeled PA were mixed at 2−200 nM, and FRET was monitored over 15 min. No increase in FRET was observed (Figure 4). When LF_N was added to initiate oligomer formation, there was a significant increase in fluorescence emission ratios, indicating that PA_{63} oligomerizes under these experimental conditions in the presence of LF_N. We conclude, however, that no significant population of oligomeric states

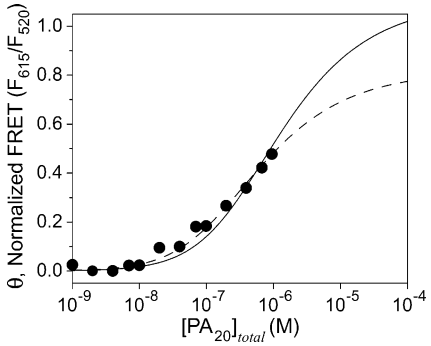

FIGURE 5: Determination of PA_{20} affinity for PA_{63} by serial dilution of nPA_{83}. An equimolar mixture nPA_{83} E465C*488 and nPA_{83} Q140C*594 was diluted to a final concentration of 1 μM to 1 nM. The observable emission ratio from the FRET pair, θ, is plotted as a function of $[PA_{20}]_{total}$ and fit to eq 2. Two fits are show where parameters are provided from kinetic measurements as fixed parameters: K_d and K_{iso} are fixed (solid line) and K_{iso} is fixed (dashed line). When the K_d is a free parameter, it fits to 90 ± 10 nM.

was formed under the conditions of our kinetic measurements.

Equilibrium Affinity of the PA_{20}·PA_{63} Interaction. To estimate the equilibrium dissociation constant, doubly labeled nPA_{83} complex was serially diluted to final concentrations from 1 nM to 1 μM and monitored by the fluorescence emission ratio, or θ (Figure 5). Due to experimental limitations, we were unable to determine a ratio for completely bound PA_{20}·PA_{63} complex (θ_{max}). While θ_{max} could be estimated from initial FRET ratios obtained in rapid dilution dissociation experiments previously described, fixed parameters determined kinetically, K_d and K_{iso}, were included in the fit to simply demonstrate consistency in the equilibrium results (Figure 5). The data were fitted to a single-site binding model in which the binding partner PA_{63} is in equilibrium with a form that is unable to bind PA_{20}, called PA_{63}* (eqs 1 and 2; see Materials and Methods). This analysis showed consistency between the equilibrium dissociation curve and kinetically determined equilibrium constants, K_d and K_{iso}. When we allowed the equilibrium K_d value to vary, it fit to 90 ± 10 nM, which suggests that nPA_{83} is mostly associated at 10 μM and mostly dissociated at 1 nM.

Temperature Dependence of PA_{20}'s Dissociation Rate. Finally, additional thermodynamic parameters for the dissociation of the PA_{20}·PA_{63} complex were obtained from temperature studies. Off-rates were determined at temperatures between 10 and 37 °C (Figure 6). The free energy of activation, $\Delta^{\ddagger}G$, for the dissociation, 19.1 kcal mol^{-1}, is large and positive, with significant contributions from both $\Delta^{\ddagger}H$ and $\Delta^{\ddagger}S$. An enthalpic barrier, as observed, is expected since unfavorable van der Waals interactions can be experienced in the process of dissociation. The observed entropic barrier may reflect freezing of rotational and/or vibrational degrees of freedom that are required during dissociation.

DISCUSSION

We have examined the kinetics and thermodynamics of the PA_{20}·PA_{63} interaction in solution using FRET between acceptor and donor fluorophores introduced into the two fragments. As PA_{83} contains no Cys residues, we used two single-Cys forms at sites that do not affect toxin activity (*21*). PA_{83}E465C was labeled with Alexa fluor 488 (donor), and

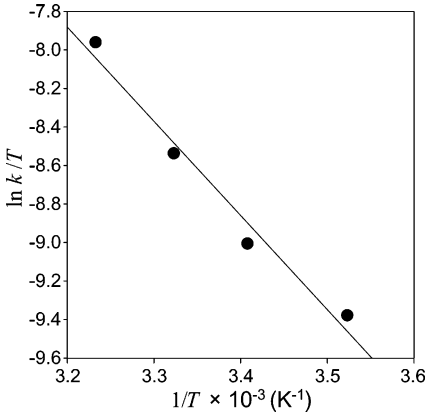

FIGURE 6: Eyring plot of complex dissociation. Off-rates of PA_{20} were measured between 10 and 37 °C and fitted by eq 3, yielding a $\Delta^{\ddagger}H$ of 9.1 ± 0.1 kcal mol^{-1}, $\Delta^{\ddagger}S$ of 33 ± 1 cal mol^{-1} K^{-1}, and a $\Delta^{\ddagger}G$ of 19.1 kcal mol^{-1} at 25 °C.

Scheme 1: Single-Site Binding Model

$$nPA_{83} \underset{k_{-1}}{\overset{k_1}{\rightleftharpoons}} PA_{20} + PA_{63}$$

Scheme 2: Encounter Complex Model

$$nPA_{83} \underset{k_{-1}}{\overset{k_1}{\rightleftharpoons}} nPA_{83}^{*} \underset{k_{-2}}{\overset{k_2}{\rightleftharpoons}} PA_{20} + PA_{63}$$

PA_{83}Q140C with Alexa fluor 594 (acceptor). The distance between Q140 and E465 in the crystallographic structure of PA_{83} is approximately 40 Å. We estimate that the Förster distance for the two dyes is 55 Å, thereby allowing for the fragment binding to be effectively reported by FRET (*20*, *22*). PA_{83} can be cleaved at, or near, the furin site with either trypsin (*23*) or furin (*24*) to generate the 20 and 63 kDa fragments. While the resulting PA_{20} fragment from trypsinization was ~3 kDa smaller than expected, the truncations were in unstructured, disordered regions of PA_{83}'s structure (Figure 1B,C; Table 1)(*9*).

Initial measurements of PA_{20}'s dissociation rate both by competition with unlabeled PA_{20} and rapid dilution suggested a simple mechanism of dissociation as shown in Scheme 1. Our data demonstrate that dissociation of the PA_{20}·PA_{63} complex is a two-step process, where the slow step is independent of concentration and likely a unimolecular rearrangement. Several potential mechanisms may manifest in the observed two-step association kinetics. One alternative (Scheme 2) is that, after nicking, the high affinity complex undergoes a slow conformational change in relative orientation (i.e. differences in the angles of the two proteins relative to each other) or other conformational rearrangements to a lower affinity transitory, encounter complex (nPA_{83}*), which then quickly dissociates (*25*, *26*). The presence of a transitory complex followed by a unimolecular rearrangement should, however, give rise to a K_d for the weak complex significantly below that determined by equilibrium measurements. This was not what we found; the equilibrium K_d measured for the PA_{20}·PA_{63} complex was within a factor of 2 of that determined kinetically, and hence, does not support a weakly associated intermediate complex. Moreover, the slow unimolecular association rate we measured is ~3.5×10^{-3} s^{-1}, and for K_d's from kinetics and equilibrium studies to be equivalent (or nearly so), the observed dissociation rate, ~3×10^{-2} s^{-1}, is 1 order of magnitude off of the expected value for Scheme 2 to be operant.

Scheme 3: Isomerization Model

$$nPA_{83} \underset{k_{-1}}{\overset{k_1}{\rightleftharpoons}} PA_{20} + PA_{63} \underset{k_{-2}}{\overset{k_2}{\rightleftharpoons}} PA_{63}^{*}$$

Scheme 4: PA_{63} Oligomerization Model

$$7\ PA_{63}^{*} \longrightarrow [PA_{63}^{*}]_7$$

A more likely alternative (Scheme 3) is that the initial dissociation of the nPA_{83} complex is followed by a rate-determining isomerization (*27*). It is known that PA_{63} in the heptameric prepore form shows differences in conformation from that observed in intact PA_{83} (*9*). Hence, the conformational change must occur in PA_{63} at some point after dissociation, to create an oligomerization-competent PA_{63}, called PA_{63}^{*}. The slow unimolecular process we observed (~3.5×10^{-3} s^{-1}) in the association kinetics (Figure 3) most likely corresponds to k_{-2} in Scheme 3. Therefore, we propose that, prior to oligomerization, PA_{63} exists in equilibrium between two conformational states, only one of which will combine with PA_{20} to form the PA_{20}·PA_{63} complex, and that the slow kinetic step observed reflects back isomerization: PA_{63}* → PA_{63}. If we speculate that PA_{63}* is, in fact, an oligomerization competent form, then the known conformational change must occur after PA_{20} dissociation, but prior to oligomerization of PA_{63}^{*}, leading to the heptamer (Scheme 4).

It follows then that we can estimate the rate constant, k_2, for the forward isomerization process, PA_{63} → PA_{63}*. Because we know both the isomerization equilibrium constant, K_{iso}, and k_{-2}, then k_2 is ~7.4×10^{-3} s^{-1}. Of more relevance to the biology of PA heptamer assembly is that the proposed isomerization, PA_{63} ↔ PA_{63}*, has as equilibrium constant of ~2.1, which favors PA_{63}* such that 68% of the PA_{63} monomers would be poised for oligomerization. Furthermore, regardless as to whether PA_{63}* is the hypothetical oligomerization competent form, the net effect of an isomerization reaction favoring PA_{63}* is that it effectively drives the dissociation of PA_{20}.

We measured a 21 s half-life for PA_{20}'s dissociation from PA_{63}. Kinetic data have been obtained for several steps of toxin assembly. The association rate for PA_{83} binding to the anthrax toxin receptor CMG2 is 1×10^5 M^{-1} s^{-1} (*19*). Elliot et al. have measured kinetics of binding of EF and LF to assembled PA heptamer with an association rate of 1.8×10^5 M^{-1}s^{-1} (*10*). Since oligomerization of PA even in the presence of LF_N (Figure 4) is slower than the relatively rapid dissociation kinetics of PA_{20}, the dissociation of PA_{20} from PA_{63} is likely not the rate-limiting step in the overall mechanism. Rather the proposed isomerization, PA_{63} ↔ PA_{63}*, may, in fact, limit heptamerization, since it is an order of magnitude slower.

We have measured kinetic and equilibrium K_d's for the PA_{20}·PA_{63} interaction, which indicate a two-step binding model. These data aid in understanding the kinetic pathway of toxin assembly. Following receptor binding and proteolytic activation, PA_{20} rapidly dissociates. A slow isomerization step in PA_{63} may then potentiate it for oligomerization in the presence of the enzymatic ligands, LF and EF. Future work will address whether oligomerization of PA_{63} is, in fact, limited by such a slow conformational rearrangement.

ACKNOWLEDGMENT

K.A.C. thanks P. Christine Ackroyd for helping prepare and critically evaluate this manuscript. We also thank Ruth-Anne L. Pimental for helping with protein production and Harvard's Microchemistry Facility for performing Edman N-terminal sequencing and mass spectrometry analyses.

REFERENCES

1. Smith, H., and Stoner, H. B. (1967) Anthrax toxic complex, *Fed. Proc. 26*, 1554−1557.
2. Smith, H. (2000) Discovery of the anthrax toxin: the beginning of in vivo studies on pathogenic bacteria, *Trends Microbiol. 8*, 199−200.
3. Duesbery, N. S., Resau, J., Webb, C. P., Koochekpour, S., Koo, H. M., Leppla, S. H., and Vande Woude, G. F. (2001) Suppression of ras-mediated transformation and inhibition of tumor growth and angiogenesis by anthrax lethal factor, a proteolytic inhibitor of multiple MEK pathways, *Proc. Natl. Acad. Sci. U.S.A. 98*, 4089−4094.
4. Pellizzari, R., Guidi-Rontani, C., Vitale, G., Mock, M., and Montecucco, C. (2000) Lethal factor of Bacillus anthracis cleaves the N-terminus of MAPKKs: analysis of the intracellular consequences in macrophages, *Int. J. Med. Microbiol. 290*, 421−427.
5. Vitale, G., Pellizzari, R., Recchi, C., Napolitani, G., Mock, M., and Montecucco, C. (1998) Anthrax lethal factor cleaves the N-terminus of MAPKKs and induces tyrosine/threonine phosphorylation of MAPKs in cultured macrophages, *Biochem. Biophys. Res. Commun. 248*, 706−711.
6. Bradley, K. A., Mogridge, J., Mourez, M., Collier, R. J., and Young, J. A. (2001) Identification of the cellular receptor for anthrax toxin, *Nature. 414*, 225−229.
7. Scobie, H. M., Rainey, G. J., Bradley, K. A., and Young, J. A. (2003) Human capillary morphogenesis protein 2 functions as an anthrax toxin receptor, *Proc. Natl. Acad. Sci. 100*, 5170−5174.
8. Klimpel, K. R., Molloy, S. S., Thomas, G., and Leppla, S. H. (1992) Anthrax toxin protective antigen is activated by a cell surface protease with the sequence specificity and catalytic properties of furin, *Proc. Natl. Acad. Sci. 89*, 10277−10281.
9. Petosa, C., Collier, R. J., Klimpel, K. R., Leppla, S. H., and Liddington, R. C. (1997) Crystal structure of the anthrax toxin protective antigen, *Nature. 385*, 833−838.
10. Elliott, J. L., Mogridge, J., and Collier, R. J. (2000) A quantitative study of the interactions of Bacillus anthracis edema factor and lethal factor with activated protective antigen, *Biochemistry 39*, 6706−6713.
11. Mogridge, J., Cunningham, K., and Collier, R. J. (2002) Stoichiometry of anthrax toxin complexes, *Biochemistry 41*, 1079−1082.
12. Abrami, L., Liu, S., Cosson, P., Leppla, S. H., and van der Goot, F. G. (2003) Anthrax toxin triggers endocytosis of its receptor via a lipid raft-mediated clathrin-dependent process, *J. Cell Biol. 160*, 321−328.
13. Milne, J. C., and Collier, R. J. (1993) pH-dependent permeabilization of the plasma membrane of mammalian cells by anthrax protective antigen, *Mol. Microbiol. 10*, 647−653.
14. Blaustein, R. O., Koehler, T. M., Collier, R. J., and Finkelstein, A. (1989) Anthrax toxin: channel-forming activity of protective antigen in planar phospholipid bilayers, *Proc. Natl. Acad. Sci. U.S.A. 86*, 2209−2213.
15. O'Brien, J., Friedlander, A., Dreier, T., Ezzell, J., and Leppla, S. (1985) Effects of anthrax toxin components on human neutrophils, *Infect. Immun. 47*, 306−310.
16. Bernard, A., and Payton, M. (1995) in *Current Protocols in Protein Science* (Coligan, J. E., Dunn, B. M., Plough, H. L., Speicher, D. W., and Wingfield, P. T., Eds.) pp 1−18, John Wiley & Sons, Inc., New York.
17. Miller, C. J., Elliott, J. L., and Collier, R. J. (1999) Anthrax protective antigen: prepore-to-pore conversion, *Biochemistry 38*, 10432−10441.
18. Lacy, D. B., Mourez, M., Fouassier, A., and Collier, R. J. (2002) Mapping the anthrax protective antigen binding site on the lethal and edema factors, *J. Biol. Chem. 277*, 3006−3010.
19. Wigelsworth, D. J., Krantz, B. A., Christensen, K. A., Lacy, D. B., Juris, S. J., and Collier, R. J. (2004) Binding Stoichiometry and Kinetics of the Inteaction of a Human Anthrax Toxin Receptor, CMG2, with Protective Antigen, *J. Biol. Chem. 279*, 23349−23356.
20. Lakowicz, J. R. (1999) *Principles of Fluorescence Spectroscopy*, 2nd ed., Kluwer Academic/Plenum Publishers, New York.
21. Mourez, M., Yan, M., Lacy, D. B., Dillon, L., Bentsen, L., Marpoe, A., Maurin, C., Hotze, E., Wigelsworth, D., Pimental, R. A., Ballard, J. D., Collier, R. J., and Tweten, R. K. (2003) Mapping dominant-negative mutations of anthrax protective antigen by scanning mutagenesis, *Proc. Natl. Acad. Sci. 100*, 13803−13808.
22. Wu P. G., and Brand L. (1994) Resonance Energy Transfer: Methods and Applications, *Anal. Biochem. 218*, 1−13.
23. Novak, J. M., Stein, M. P., Little, S. F., Leppla, S. H., and Friedlander, A. M. (1992) Functional characterization of protease-treated Bacillus anthracis protective antigen, *J. Biol. Chem. 267*, 17186−17193.
24. Molloy, S. S., Bresnahan, P. A., Leppla, S. H., Klimpel, K. R., and Thomas, G. (1992) Human furin is a calcium-dependent serine endoprotease that recognizes the sequence Arg-X−X-Arg and efficiently cleaves anthrax toxin protective antigen, *J. Biol. Chem. 267*, 16396−16402.
25. Beckingham, J. A., Bottomley, S. P., Hinton, R., Sutton, B. J., and Gore, M. G. (1999) Interactions between a single immunoglobulin-binding domain of protein L from *Peptostreptococcus magnus* and a human κ light chain, *Biochem. J. 340*, 193−199.
26. Wallis, R., Moore, G. R., James, R., and Kleanthous, C. (1995) Protein−Protein Interactions in Colicin E9 DNase- -Immunity Protein Complexes. 1. Diffusion-Controlled Association and Femtomolar Binding for the Cognate Complex, *Biochemistry 34*, 13743−13750.
27. Joshi, R. V., Zarutskie, J. A., and Stern, L. J. (2000) A Three-Step Kinetic Mechanism for Peptide Binding to MHC Class II Proteins, *Biochemistry 39*, 3751−3762.

BI047791S